Mitocytosis Mediated by an Enzyme-activable Mitochondrion-disturbing Polymer-drug Conjugate Enhances Active Penetration in Glioblastoma Therapy

Yufan Xiang, Bing Wang, Wanchun Yang, Xiuli Zheng, Rongjun Chen, Qiyong Gong, Zhongwei Gu, Yanhui Liu and Kui Luo**

Dr. F. Xiang, Dr. B. Wang, Dr. W. Yang, Dr. X. Zheng, Prof. Q. Gong, Prof. Z. Gu, Prof. Y. Liu, Prof. K. Luo

Department of Neurosurgery, Department of Radiology, Neurosurgery Research Laboratory, Huaxi MR Research Center (HMRRC), Frontiers Science Center for Disease-Related Molecular Network, State Key Laboratory of Biotherapy, West China Hospital, Sichuan University, Chengdu 610041, China.

*E-mail: luokui@scu.edu.cn (Prof. Luo), liuyh@scu.edu.cn (Prof. Liu)

Prof. R. Chen

Department of Chemical Engineering, Imperial College London, South Kensington Campus, London SW7 2AZ, UK

Prof. Q. Gong, Prof. K. Luo

Functional and Molecular Imaging Key Laboratory of Sichuan Province, and Research Unit of Psychoradiology, Chinese Academy of Medical Sciences, Chengdu 610041, China

Prof. Q. Gong

Department of Radiology, West China Xiamen Hospital of Sichuan University, Xiamen 361021, China

Keywords: Nanomedicine, mitochondrion targeting, mitocytosis, tumor penetration, glioblastoma

Abstract: The application of nanomedicines for glioblastoma (GBM) therapy is hampered by the blood-brain barrier (BBB) and the dense glioblastoma tissue. To

achieve efficient BBB crossing and deep GBM penetration, we demonstrated a strategy of active transcellular transport of a mitochondrion-disturbing nanomedicine, GBEPPT, in the GBM tissue through mitocytosis. GBEPPT was computer-aided designed and prepared by self-assembling a conjugate of an amphiphilic block polymer and a drug podophyllotoxin (PPT). When GBEPPT was delivered to the tumor site, overexpressed γ-glutamyl transpeptidase (GGT) on the brain-blood endothelial cell or the GBM cell triggered enzymatic hydrolysis of γ-glutamylamide on GBEPPT to reverse its charge. Positively-charged GBEPPT rapidly entered into the cell and targeted the mitochondria. These GBEPPT disturbed the homeostasis of mitochondria, inducing mitocytosis-mediated extracellular transport of GBEPPT to the neighboring cells via mitosomes. This intracellular-to-intercellular delivery cycle allowed GBEPPT to penetrate deeply into the GBM parenchyma, and exert sustainable action of PPT released from GBEPPT on the tumor cells along its penetration path at the tumor site, thus improving the anti-GBM effect. The process of mitocytosis mediated by the mitochondrion-disturbing nanomedicine may offer great potential in enhancing drug penetration through malignant tissues, especially poorly permeable solid tumors.

1. Introduction

Treatment of glioblastoma (GBM) meets the challenge of crossing the blood-brain barrier (BBB).[1] Although intact and impaired BBBs coexist at the GBM site, a restrictive physiological and functional barrier prevents sufficient exposure of an anti-GBM drug to parenchymal brain tissues to exert its therapeutic effect.[2] Only a few drugs are capable of passive diffusion though the BBB, such as lipophilic drugs, but they usually exhibit poor penetration into brain tumor tissues, necessitating high drug dosages that may result in dose-limiting systemic toxicity.[3] Active transport strategies based on novel biomaterials have been developed to address the shortcomings of passive drug transports across the BBB. A recent finding suggests that an active BBB-crossing mechanism via caveolin-1-dependent transcytosis enhances the penetration of drugs through the BBB to a brain tumor tissue,[4] revealing that the active transcellular

transport behavior may be an essential aspect to consider when constructing a drug delivery system (DDS) across the BBB.

Another obstacle in GBM treatment is drug transportation to an extravascular distant region at the GBM site.[5] Anchoring targeted small molecules, peptides or proteins to the surface of a DDS increases the aggregation of the DDS in GBM, but deep penetration of the DDS remains a challenge.[6] Previously, we designed a tumor microenvironment-responsive peptide polymeric DDS for deep tumor penetration via membrane flow.[7] The released agents were efficiently embedded in the bilayer of endoplasmic reticulum (ER) membranes and the lipid raft of tumor cell membranes to disturb their homeostasis, which successfully enabled intracellular transport, intercellular delivery and deep penetration of the drug through cellular membrane flow in solid tumor tissues. Accordingly, the intracellular organelles could be targeted to induce transcellular transfer of nanoformulations for a high degree of drug penetration within GBM.

Herein, prompted by the overexpression of gamma-glutamyl transpeptidase (GGT) on both the BBB neovasculature and GBM cells,[8] we designed and synthesized a GGT-responsive amphiphilic block polymer-drug conjugate, pGBEMA$_{22}$-*b*-pSSPPT$_9$ (GBEPPT), as a self-assembled nanomedicine, and its performances of BBB crossing and GBM penetration were evaluated. GBEPPT was derived from podophyllotoxin (PPT), an anti-tumor drug for inhibiting microtubule polymerization, and N^5-(1-((2-methacrylamidoethyl)amino)-1-oxobutan-2-yl)glutamine (GBEMA), a monomer containing a glutathione analogue for GGT cleavage. The chemical structure of GBEPPT was optimized through dissipative particle dynamics (DPD) simulations. It is found that GBEPPT could rapidly aggregate in the mitochondria and disturb mitochondrial homeostasis to mediate mitocytosis, a mitochondrial quality-control process. In an in-situ inoculated GBM mouse model, mitocytosis could promote active delivery of GBEPPT in a GBM microenvironment to realize penetration across the BBB and through the GBM tissue. The nanomedicine exhibits potent tumor cell inhibition at a low dose and a significant anti-GBM effect *in vivo*, and simultaneously

attenuates the lethal systematic toxicity of PPT. These findings suggest mitocytosis could play a pivitol role in the enhanced permeation through both the BBB and the GBM issue after treatment with the mitochondria-disturbing nanomedicine, providing a new avenue for active transcellular transport of drugs into brain tumors (**Scheme 1**).

2. Results and Discussion

2.1. Design, Synthesis, and Characterizations

Inefficient drug delivery into the GBM tissue has been one of the major culprits to treatment failure, recurrence, and poor survival of GBM patients.[1,9] A better understanding of the membranal molecular characteristics of the brain tumor tissue may propel the development of novel drug delivery strategies. Western blot (WB) analysis of GBM cells, primary astrocytes, brain tumor tissues and the contralateral normal brain tissue reveals that there is an upregulated expression level of GGT in the brain tumor tissue (Figure S1, Supporting Information). Previous studies have confirmed that the BBB in the GBM site exhibits a high expression level of GGT.[8a,b,10] Therefore, a drug delivery system could be designed to target GGT for efficient penetration in GBM. As shown in **Figure 1**a, the designed amphiphilic polymer contains a hydrophilic unit, which includes a GGT-responsive charge-reversal segment (γ-glutamine) that is conjugated to a positively-charged provider (aminobutyric acid), and a hydrophobic domain, which is composed of a GSH-responsive linker and an anti-tumor drug, PPT.

In addition to the chemical structure of an amphiphilic polymer, the structural morphology of an assembled nanomedicine is essential for its stability, biodistribution and penetration *in vivo*.[11] Dissipative particle dynamic (DPD) simulation has been widely employed to examine morphological changes of amphiphilic polymers during the self-assembly process.[12] Therefore, the self-assembly process of the amphiphilic polymer-drug conjugate at a pre-determined hydrophilic-hydrophobic ratio was simulated via DPD and the simulation results guide the synthesis of the amphiphilic conjugate (Figure 1b, Figure S2-S7, and Table S1, Supporting Information). The amphiphilic polymer-drug conjugates at eight different ratios of hydrophilic to hydrophobic units were initially selected to assemble to form small aggregated clusters

and the clusters gradually fuse with each other to evolve into larger assemblies. After 180,000 simulation steps, seven out of these eight conjugates are found to transform into independent assemblies, while one conjugate at the same number of hydrophilic and hydrophobic units (x = 15, y = 15) finally reaches an independent assembly after 320,000 simulation steps (Figure S3 and S4, Supporting Information). Although the assembled morphologies of these conjugates remain unaltered as the simulation steps increase, they vary quite dramatically at different hydrophilic-hydrophobic ratios in the amphiphilic conjugates (Figure 1b and Figure S5, Supporting Information). Notably, the morphological shape of the final assembly changes from a cylinder to a nanosphere, and then from a nanosphere to a cylinder as the ratio of hydrophilic-hydrophobic units increases. A cylindrical morphology with a large size may be ineffective for drug delivery into the glioma, while the nanosphere assembly with an appropriate size could be more favorable.[13] The total potential energy of these assemblies decreases during the assembly process and remains at a constant and low level after self-assembly, indicating that each system is able to enter into a dynamically balanced assembling state (Figure S6, Supporting Information). The hydrophobic drug PPT is wrapped with the hydrophilic unit in each assembly according to the radial distribution function (RDF) curves (Figure S7, Supporting Information). Based on the morphologies of the assembly and the shifts in the total energy during the assembly process, a ratio of hydrophilic to hydrophobic units is selected to be ≈1-4 (x/y ≈ 1-4) for synthesizing the amphiphilic conjugate.

Guided by DPD simulation results, the targeted amphiphilic block polymer-drug conjugate, pGBEMA$_{22}$-*b*-pSSPPT$_9$ (GBEPPT), was synthesized according the routes in Figure S8, Supporting Information, and the conjugate could self-assemble into a stable nanomedicine in an aqueous solution with a critical micelle concentration (CMC) of 2.29 μg mL^{-1} (Figure 1d). Detailed synthesis procedures and characterizations are shown in Figure S9-S27, Supporting Information. The ratio of hydrophilic to hydrophobic units in GBEPPT is determined to be 2.4 by gel permeation chromatography (GPC, Figure 1c), which falls within the ratio range recommended

from the simulation results and is aligned with the integral ratio of the characteristic peaks for the hydrophilic and hydrophobic units in the NMR spectrum (Figure S27, Supporting Information). A control polymer, $pGEMA_{20}$-*b*-$pSSPPT_8$ (GEPPT) without L-α-aminobutyric acid in the hydrophilic segment, was also synthesized and characterized (Figure S28 to S36, Supporting Information). GBEPPT has a hydrodynamic size of 52.76 nm and a polydispersity index (PDI) of 0.116 via dynamic light scattering (Figure 1e), and this size falls within the size range of 20-70 nm of typical nanocarriers for crossing the BBB.[14] The size and PDI of GBEPPT in PBS have negligible changes over a period of 96 h, suggesting that this nanoparticle is able to maintain a stable self-assembled structure for a long duration (Figure 1f). Due to its structural resemblance to GBEPPT, GEPPT also has a very stable nanostructure which is confirmed from the CMC and DLS assays, as shown in Figure S37-S39, Supporting Information.

DPD simulations were further conducted to investigate the GGT-responsive process of GBEPPT. As shown in Figure 1g and Figure S40-S42, Supporting Information, a stable nanosphere-assembly structure could be formed after 2,000,000 steps of simulation. Upon the addition of an enzyme, γ-glutamine is continuously shed from the surface of GBEPPT with an increase in the simulation step. However, this bond-breaking process does not result in an evident change in the assembly morphology of GBEPPT, and the morphology is maintained even after 4,000,000 simulation steps. Meanwhile, the total potential energy of the nanosphere is almost a constant throughout the γ-glutamine shedding process (Figure S43, Supporting Information). The interaction between each constitutional block and PPT (E-P, A-P, D-P and P-P) remains almost identical in the RDF curves, however, the interaction between γ-glutamine and PPT (G-P) decreases dramatically (Figure S44, Supporting Information). The exposed amino group generated from the cleavage of γ-glutamine has a similar hydrophilic level as γ-glutamine, thus maintaining a similar hydrophilic to hydrophobic balance as the original GBEPPT, therefore, the resulting nanostructure stays spherical. The TEM images confirm a nanosphere structure of GBEPPT after enzymatic treatment,

supporting the simulation results (Figure 1h and 1i). The DLS data reveals that the particle size increases marginally after enzyme treatment (Figure S45, Supporting Information). Similar findings are obtained for the control polymer, GEPPT, after enzymatic treatment (Figure S46 and S47, Supporting Information). As the enzymolysis of γ-glutamylamide produces an amino group for protonation, the surface charges of GBEPPT and GEPPT were monitored throughout the enzyme hydrolysis. After incubation with 10 U mL^{-1} of GGT in PBS (pH 7.4), the surface charge of GBEPPT reverses from -6.84 to 4.58 mV, while the surface charge of GEPPT remains negative despite a rise in the surface charge (Figure 1j). The charge-reversal characteristic of GBETPPT triggered by GGT could be favorable for cellular endocytosis in the tumor tissue.

RP-HPLC was used to examine the glutathione (GSH)-responsive drug release process from the nanomedicine after incubation with or without GSH (Figure S48, Supporting Information). The amount of PPT released in the absence of GSH is negligible, while after GSH treatment, a typical peak of PPT is seen in the HPLC chromatogram, supporting responsive drug release from the nanomedicine and confirming the same structure of the released PPT as that of free PPT. The PPT content in GBEPPT and GEPPT is determined to be 16.9% and 18.1%, respectively, by RP-HPLC. Drug release profiles from GBEPPT were then conducted at a GSH concentration gradient (Figure 1k). At a physiological GSH concentration (0.01 mM), co-incubation of GBEPPT and GSH for 24 h results in the release of 17.7% of PPT from GBEPPT, indicating that GBEPPT could remain stable in the blood circulation system or normal tissues and release a considerably small amount of PPT, thus reducing its side effects. The PPT release efficiency is enhanced when the GSH concentration increases in the extracellular matrix of the tumor tissue (0.1 mM). At a GSH concentration inside tumor cells (10 mM),[15] the release rate of PPT is determined to be 82.2% after 24 h, suggesting that GBEPPT can selectively release the drug in cancerous cells to exert its therapeutic effect. Because the GSH-responsive linker for PPT in GEPPT is the same as that in GBEPPT, at a GSH concentration of 10 mM, a

similar amount of PPT (79.7%) is released from GEPPT after 24 h, as shown in Figure S49, Supporting Information. The degradability of GBEPPT was examined using GPC. After 48 h of incubation with GGT and dithiothreitol, GBEPPT is degraded to yield pBE-*b*-pSH, a hydrophilic product (Figure S50, Supporting Information) with a low molecular weight of 5.2 kDa, which is far below the threshold for renal excretion of polymers. The blood of the mice was collected for chemical index analysis on day 7 post *i.v.* injection of GBEPPT. All biochemical indicators for the serum are within the normal ranges. There is no significant difference in these indicators between the GBEPPT group and the control group, implying that GBEPPT is hemo-compatible (Figure S51, Supporting Information).

2.2. Internalization and organelle localization

To track the internalization behaviors of both nanomedicines, Cy5-labelled GBEPPT and GEPPT were synthesized with a Cy5 content of 0.7% and 0.8%, respectively. Flow-cytometric analysis reveals that internalization of GBEPPT by U87-MG cells is time-dependent (Figure S52, Supporting Information). In comparison to GEPPT, a comparatively higher degree of internalization is found for GBEPPT into U87-MG cells (Figure S53, Supporting Information), suggesting that the GGT-responsive charge-reversal property of GBEPPT could augment the rate of its endocytosis into GBM cells. To distinguish the endocytic pathway for GBEPPT, several endocytosis inhibitors were used to pre-treat GBM cells. The experimental procedure is shown in Figure S54, Supporting Information. A low temperature of 4 °C instead of 37 °C markedly reduces cellular uptake of GBEPPT, indicating that GBEPPT enters the cells via energy-dependent endocytosis. Genistein is often used as an inhibitor for caveolae-mediated endocytosis and dynasore inhibits the dynamin-dependent endocytic pathway, while chlorpromazine and cytochalasin D inhibit clathrin-mediated endocytosis and micropinocytosis, respectively.[16] Treatment with genistein and dynasore significantly reduces the uptake of GBEPPT and the inhibition ratio is 70% and 50%, respectively. However, treatment with chlorpromazine slightly inhibits the endocytosis of GBEPPT (10%) and cytochalasin D has no endocytic inhibitory effect. In summary, the

predominant endocytic pathway for GBEPPT into GBM cells is energy-dependent caveolae-mediated endocytosis, and this process is highly supported by dynamin.

Subcellular localization of GBEPPT in GBM cells was unveiled through confocal laser scanning microscopy (CLSM). After uptake by GBM cells, a highly pronounced level of co-localization is found between GBEPPT and mitochondria with a Pearson's R of 0.85 (**Figure 2**a-c), while the level of co-localization with other organelles is insignificant, such as lysosomes with a Pearson's R of 0.31 (Figure 2d-f), the endoplasmic reticulum (ER) with a Pearson's R of 0.26 (Figure 2g-i), and the Golgi apparatus with a Pearson's R of 0.17 (Figure 2j-l). In contrast, a less substantial level of co-localization between GEPPT and mitochondria is observed in the CLSM images of the cells after uptake of GEPPT, a control without the property of GGT-responsive surface charge reversal (Figure S55, Supporting Information). The Manders' Colocalization Coefficients for GBEPPT (M_X) and major organelles (M_Y) also indicate a high level of co-localization between GBEPPT and mitochondria (Figure S56, Supporting Information). Furthermore, GBEPPT could be rapidly internalized into GBM cells and it co-localizes with the mitochondrial network within 20 min (see Video 1, Supporting Information). Semi-quantitative results from this dynamic process are depicted in Figure 2m, confirming a rapid increase in the Pearson's R for co-localization of GBEPPT and mitochondria within a short time frame. These results imply that GBEPPT can highly and swiftly aggregate in mitochondria, and this feature may be credited to the charge-reversal property of the delivery system.

To assess the impact of GBEPPT on the mitochondrial membrane potential (MMP) of mitochondria, flow cytometric analysis was conducted after JC-1 staining was applied to the mitochondria of GBM cells. Typically, JC-1 on normal mitochondria membranes displays red fluorescence as J-aggregates, while it displays green fluorescence as J-monomers after its interaction with damaged mitochondrial membranes.[17] The ratio of red/green fluorescence intensity is often used to quantitatively estimate the MMP. As shown in Figure 2n, the ratio of red/green fluorescence intensity, or the ratio of normal/damaged mitochondrial membranes,

increases in the early stage (0-1 h) and then gradually decreases (2-24 h) when the cells are incubated with GBEPPT. Simultaneously, after treatment with GBEPPT, there is a mild increase in the level of mitochondrial superoxide within the GBM cells (Figure S57, Supporting Information), and the pattern of temporal changes in cellular ATP production is similar to that of the MMP changes (Figure S58, Supporting Information). A modest level of mitochondrial disturbance could be induced by GBEPPT when it enters into the tumor cells and interacts with the mitochondria, activating the mitochondrial quality-control mechanism.[18] During the quality-control process, the disturbed mitochondria as mitosomes are secreted out of the cell to help prevent accumulation of malfunctioning mitochondria in the cell to prolong its survival. It is noted that the internalized GBEPPT may continuously interact with the mitochondrial network in the cells to promote mitochondrial secretion. Long-term GBEPPT-organelle co-localization observations reveal that the overlapping level of the fluorescence signal of GBEPPT with the mitochondrial signal displays a downward trend (Figure 2o), while the co-localization level of GBEPPT with other major organelles remains unaltered (Figure S59, Supporting Information). After incubation for 3 h, the Pearson's R of for the co-localization of GBEPPT and mitochondria decrease to 0.75, confirming that a cetain amount of GBEPPT may be transported out of the cell through mitosomes via the mitochondrial quality control process.

2.3. Mitocytosis and Intercellular Transport

Mitochondria can be secreted out of a cell via mitosomes during the process of mitocytosis. Particularly, when this organelle is mildly disturbed, mitochondrial effusion to the outside of the cell is promoted to maintain the mitochondrial homeostasis, and this mechanism is different from mitophagy, another process for regulating the mitochondrial homeostasis. When mitochondria encounter mild disturbance, mitocytosis and mitophagy can occur simultaneously, but mitocytosis is predominant. However, when mitochondria are subjected to severe damage, the occurrence of mitocytosis becomes rare.[18,19] The mitophagy level in the GBM cells treated with GBEPPT is significantly lower than that in the GBM cells treated with CCCP (Carbonyl

cyanide 3-chlorophenylhydrazone) (Figure S60, Supporting Information). There is no significant increase in the level of mitophagy with an increase in the dosage of GBEPPT. To examine whether GBEPPT accumulating in the mitochondrial network after cellular uptake could trigger mitochondrial exocytosis via the mitocytosis process, CLSM was used to undertake dynamic observations of GBM cells under a fixed field of view. After the GBM cells were pretreated with GBEPPT for 1 h and then the culture medium was replaced by a fresh one without GBEPPT, the observations were conducted for 50 min (**Figure 3**a). The green fluorescence-stained mitochondria overlap with GBEPPT with red fluorescence in the surrounding area outside of the cells (white arrow), and the level of extracellular co-localization of mitochondria and GBEPPT is augmented significantly with a prolonged incubation time. However, very few mitochondria are secreted out of the untreated cells into the extracellular area (Figure 3b and 3c). Videos for capturing the dynamics of the CLSM fluorescence signal in the field of view can be found in the Supporting Information (Video 2-8, Supporting Information). The Pearson's R for co-localization of GBEPPT and mitochondria inside GBM cells displays a steady decrease as the co-incubation duration rises (Figure 3d). These observations suggest that the mitochondria containing relatively highly aggregated GBEPPT may initially evacuate to the extracellular space via the mitocytosis process.

Transmission electron microscopy (TEM) images reveal that after co-incubation of GBM cells with GBEPPT, the mitochondria at the bottom of the GBM cells are dysfunctional (Figure 3e and Figure S61, Supporting Information) because these disturbed mitochondria appear quite different from normal mitochondria, including swelling, disruption of cristae and the formation of electron-dense aggregates. The disturbed mitochondria are also observed to accumulate in mitosomes. Different types of mitosomes are observed in terms of the mitosome volume, the number of mitochondria in mitosomes, and the number of mitosomes on the same retraction fiber. One mitosome could contain one or more disturbed mitochondria, and multiple mitosomes may share a single retraction fiber. Overall, these results suggest that mild disturbance of mitochondria by GBEPPT could activate the mitochondrial quality

control mechanism, resulting in translocation of some of disturbed mitochondria outside of the cell via mitocytosis, and GBEPPT associated with these expelled mitochondria is also transported out of the cell.

After the nanomedicine exocytoses into the extracellular space, they may be re-endocytosed by other cells to achieve intercellular transport or transcytosis.[20] In order to investigate the relationship between mitocytosis and transcytosis of GBEPPT, inhibition experiments were conducted and the experimental procedure is depicted in Figure S62, Supporting Information. Nocodazole can inhibit mitochondrial motion and the formation of the peripheral mitochondrial network, which are two key activities in the mitocytosis process.[21] Amiloride inhibits the secretion of exosomes, including mitosomes.[22] The results reveal that intercellular transport is considerably impeded at 4 °C, and the amount of GBEPPT internalized into the GBM cells decreases by 90% compared to the control group (Figure S62, Supporting Information). Nocodazole exhibits an evident inhibitory effect on intercellular transport of GBEPPT. The re-internalizated GBEPPT amount by GBM cells decreases by 50%, while amiloride demonstrates a certain degree of inhibition on intercellular transport (23%). Consequently, the mitocytosis process is an energy-dependent process that is closely associated with transcytosis.

2.4. BBB and GBM Penetration

The blood-brain barrier (BBB) is an impediment to be overcome by drugs to achieve effective anti-GBM treatment *in vivo*. We utilized bend.3 endothelial cells to construct an *in vitro* BBB model to examine the penetration of GBEPPT across the BBB (**Figure 4**a). The results support that GBEPPT could penetrate the BBB model and the amount of GBEPPT across the BBB increases with an increase in the incubation time (Figure 4b). After 4 h of incubation, the amount of GBEPPT penetrating through the BBB is equivalent to that in the control group without a BBB model (Figure 4c). Throughout the co-incubation period, GEPPT displays a lower level of penetration across the BBB than GBEPPT, which might be attributed to the fact the GGT-activated mitochondrial disturbance by GBEPPT could strengthen mitocytosis to enhance its BBB penetration.

Deep penetration of a nanomedicine in a solid tumor after crossing the BBB plays an equally critical role in inhibiting GBM.[5a,23] We employed 3D multicellular tumor spheroids (MTSs) of GBM to mimic the penetration of GBEPPT into solid GBM tumors. The CLSM images in Figure 4d and Figure S63, Supporting Information, display that GBEPPT is well distributed in the interior region of the MTSs with a diameter of around 500 μm. GEPPT, in contrast, is seen in the periphery of the MTSs rather than in their center. A line scan analysis of the fluorescence intensity from the left to right periphery of MTSs reveals that GBEPPT-treated MTSs exhibit a much stronger fluorescence intensity inside the spheroids than those treated with GEPPT (Figure 4e). Previous studies have confirmed that a tumor tissue is often located within 200 μm from neovascularization.[5b] As a result, GBEPPT has the potential to penetrate deeply into a solid tumor. After MTSs were exposed to nocodazole, we observe a noticeable decrease in the penetration depth of GBEPPT towards the center of MTSs, while there are no significant changes before and after nocodazole treatment in the GEPPT group (Figure S64, Supporting Information). These findings suggest that outstanding penetration of GBEPPT could be ascribed to mitocytosis.

Next, we examined the penetration ability of GBEPPT through the BBB *in vivo*. A single injection of luciferase-expressed U87MG (U87MG-Luc) cells into the mice caudate putamen (striatum) to build a tumor-bearing mouse model. The brain tissue and major organs harvested from the mice receiving different treatments were examined by ex vivo imaging (Figure 4f and 4g and Figure S65, Supporting Information). The mice treated with GBEPPT display distinctively stronger Cy5 fluorescence signal in the brain tissue than those treated with GEPPT or small-molecule Cy5. The relative ratio of the fluorescence intensity of Cy5 in Cy5-labelled GBEPPT over that of luciferin-expressed tumor cells in the brain tumor tissue is approximately 2.5 times higher than that in the mice treated with GEPPT (Figure 4g). These results demonstrate that GBEPPT could cross the BBB in the mice model and accumulate in the GBM tumor region at a high concentration. The images of major organs suggest that both GBEPPT and GEPPT could accumulate in the liver, spleen, and kidney. A considerable level of accumulation

of GBEPPT in the kidney may be credited to a high expression level of GGT in the renal region.[24]

We fixed and stained the sections of the GBM tissue and observed the permeation of GBEPPT and GEPPT from blood vessels to the GBM tissue. As shown in Figure 4h, the amount of GBEPPT (red) in the tumor tissue is much higher than that of GEPPT. The vast majority of GBEPPT diffuses from the blood vessels (green) into the tumor region and is evenly distributed inside the tumor tissue, whereas GEPPT is prone to co-localizing with blood vessels. Semi-quantitative analysis of the fluorescence signal from Cy5-labeled GBEPPT or GEPPT (red) in the GBM (Figure 4i) and the co-localization level of Cy5-labeled GBEPPT or GEPPT with blood vessels (green) (Figure 4j) confirms that injection of GBEPPT into a mouse bearing the GBM tumor leads to more evident tumor accumulation and permeation in the GBM compared to GEPPT, owing to its GGT-activated charge-switchable characteristics that facilitate its endocytosis into tumor cells, mitochondrial disturbance, and mitochondrial mitocytosis to enhance its transcytosis.

2.5. GBM tumor therapy

U87-MG cells were used to evaluate the cytotoxicity of GBEPPT and GEPPT. CCK-8 assays reveal that the treatment with either GBEPPT (IC50 = 233.5 nM) or GEPPT (IC50 = 250.5 nM) results in a slight reduction in cytotoxicity compared to that by free PPT (IC50 = 16.4 nM), which might be attributed to a slow drug release rate from the nanomedicines. However, even at a low dose, they have a considerable inhibitory effect on GBM cells (Figure S66, Supporting Information).

The fluorescence signal intensity of U87-luc cells was assessed. It is noted that the fluorescence intensity emitted from the cells is positively correlated the number of cells after addition of D-luciferin (Figure S67, Supporting Information), thus the fluorescence signal could be used for monitoring tumor cell growth in vivo, which lays a foundation for semi-quantitative tracking the progression of orthotopic GBM *in vivo.* Moreover, *in vivo* pharmacokinetic analysis was performed through the fluorescence signal of Cy5 labelled on GBEPPT. The blood Cy5 concentration in the free Cy5 group

(Figure S68 and Table S2, Supporting Information) drops rapidly, with an estimated elimination blood half-life of 132.4 min. Although the Cy5 content in the GBEPPT group declines considerably as well, the decreasing rate is much slower than that in the free Cy5 group. Meanwhile, its blood half-life is estimated to be 730.7 min. This prolonged circulation time may be attributed to a high molecular weight of GBEPPT, a negatively charged surface, and a nanoscale structure.

An in-situ GBM model was utilized to assess the therapeutic effect of the nanomedicine. The GBM was implanted in a non-functional area of the mouse brain (caudate-putamen). Figure S69, Supporting Information, depicts the treatment method: intravenous injections of a solution of GBEPPT, GEPPT, PPT, or PBS into a mouse through tail vein were commenced after 12 days of in-situ GBM implantation, and three injections were conducted with a gap of 4 days. The GBM volume and the mouse body weight were examined on regular intervals after the first intravenous injection. On day 29, the mice were euthanized and the collected major organs and tumors were pathologically examined.

7T MRI scans were conducted to observe the growth of intracranial GBM in each group every 7 days. As shown in **Figure 5**a, the maximal cross-sectional area of the GBM tumor in the MRI images expands after therapy in all groups, while the degree of volumetric expansion varies dramatically. The fastest growth of in-situ GBM is seen in the PBS-treated mice during the treatment period. Inhibition of GBM growth is observed in the early phase in both groups administrated with PPT and GEPPT, whereas pronounced suppression of GBM growth is found in the GBEPPT-treated group during the entire treatment period. Importantly, except for the animals treated with GBEPPT, the brain tissue of the mice in other groups displays a considerable midline shift due to tumor compression after 28 days.

In vivo fluorescent imaging during the treatment period was also performed for quantitative determination of in-situ GBM growth. We monitored the fluorescence intensity of the implanted GBM-luc cells and implemented semi-quantitative analysis of the tumor volume after injection of the luciferin substrate into the mice via tail vein

at 20 min before detection (Figure 5b-d). Except for the GBEPPT-treated group, the other groups do not display noticeable inhibition of GBM during the drug administration phase (day 1 to day 13), and GBM in these groups begins to grow when the drug administration is discontinued. The most rapid growth of GBM is seen in the groups treated with PBS and GEPPT, indicating that *i.v.* administrated GEPPT does not exert an anti-tumor effect on in-situ GBM. In contrast, the mice administrated with GBEPPT exhibit significant inhibition of in-situ GBM throughout the entire monitoring period including after termination of drug administration, indicating that GBEPPT could successfully cross the BBB, transport into the GBM tumor, and retain in the tumor site for a long time to exert a long-lasting anti-GBM effect. It is noticed that during the period after termination of the treatment, the growth of GBM in the PPT-treated group is slower than that in the groups treated with PBS and GEPPT. This may be owing to the formulation of the PPT injectable solution, which contains a mixture of ethanol and castor oil. This formulation may increase the solubility of PPT in the formulation to facilitate its penetration through the BBB to the tumor site, resulting in GBM suppression.[25] However, its inhibitory effect lasts for a short time. Importantly, no significant changes in the body weight are noticed in all these groups during the treatment period (Figure 5e).

To further assess the therapeutic effect in each group, slices of tumor tissues and major organs were subjected to hematoxylin and eosin (H&E), terminal deoxynucleotidyl transferase-mediated dUTP nick-end labeling (TUNEL) and Ki67 staining. No significant abnormalities are found in the major organs (heart, liver, spleen, lung, kidney, and normal brain) after H&E staining (Figure S70 and S71, Supporting Information) with the exception of those in the PPT-treated group. Expanded nuclei, a lower hepatocytic density, and dilated hepatic blood sinusoids are observed in the liver slices after PPT treatment, suggesting that PPT administrated via tail vein injection has serious side effects, while conjugation of PPT to a nanocarrier to form a nanomedicine could significantly lessen its adverse effects. The cell density of the tumor tissues in the GBEPPT-treated group is lower than that in other groups after they were stained with

H&E (Figure S71, Supporting Information). Additionally, the tumor growth index, Ki67, is much lower, whereas the cell apoptosis index, TUNEL, is significantly greater in the GBEPPT-treated group compared to those in other groups (Figure 5f-i). Hence, it can be concluded that GBEPPT could precisely deliver PPT to the brain tumor and elicit a discernible inhibitory effect on the proliferation of GBM.

In the survival experiment, we treated the mice with in-situ GBM using the same administration method in Figure S69, Supporting Information. Significant side effects of PPT result in the death of half of the mice (5 mice) in the next day after the third *i.v.* drug administration. The other half of the mice that manage to survive may be impacted by acute toxicity of PPT, and its therapeutic action on the GBM leads to the suppression of GBM growth.[26] The final statistical results reveal that the mice exposed to PBS, PPT and GEPPT exhibit a median survival of 33, 38 and 39 days, respectively. Encouragingly, treatment with GBEPPT significantly prolongs the survival time to 46 days compared to other formulations (Figure 5j). These results strongly support the superior performance of GBEPPT in inhibiting tumor growth and prolonging the survival of the GBM-bearing mice.

2.6 Anti-tumor mechanism

A thorough investigation was conducted to gain a deeper understanding of the anti-tumor mechanism of the mitochondria-disturbing GBEPPT. It has been shown that PPT is a highly effective anti-tumor drug to impair microtubule depolymerization properties.[26a,b,27] After co-incubation with GBEPPT for 6 h, the GBM cells display multilevel cellular shrinkage (Figure S72, Supporting Information), and some of the shrunken cells have already undergone cell death (Figure S73 and S74, Supporting Information). Structured illumination microscopy (SIM) images reveal that the microtubules of GBM cells crumple and their structural integrity is disrupted after treatment with GBEPPT, which is similar to that after treatment with free PPT, implying that GBEPPT could effectively release PPT to exert a distinctive microtubule-disrupting effect on GBM cells in a high GSH concentration microenvironment (**Figure 6**a and Figure S75 and S76, Supporting Information). The mitotic process of GBM cells

is disturbed after the disruption of the microtubule structural integrity. Flow cytometry analysis reveals that the cell cycle of the majority of GBM cells is arrested at the G2/M phase after the treatment with GBEPPT or PPT, while the number of cells in the G1 and S phases is significantly reduced compared to the control (Figure 6b). Despite its high targetability towards the mitochondria, GBEPPT displays a similar inhibitory effect against tumor cells as PPT, which does not possess the mitochondrial targeting ability. The impact of GBEPPT-induced mitochondrial disturbance does not prominently contribute to the inhibition of tumor cell growth.

Transcriptome sequencing was conducted on GBM cells to investigate the role of GBEPPT in the process of cell death. The Heatmap analysis shows significant changes in the gene transcription levels of U87 cells after their co-incubation with PPT and GBEPPT, compared to the control group (Figure 6c). However, the groups treated with PPT and GBEPPT share similar alterations at the gene transcription level. In the volcano plot, significant changes are found for certain apoptosis-related genes (Figure 6d). Additionally, the GO enrichment analysis reveals a significant enrichment of genes with an altered expression level for the apoptotic pathway (Figure 6e). In the GSEA analysis, both groups treated with PPT and GBEPPT exhibit the most pronounced enrichment in the apoptotic process (GO:0006915), and the enrichment scores for both groups have a very similar trend (Figure 6f). Consequently, after cell cycle arrest and disruption of microtubule-associated cellular structures, GBM cells are prone to death via the apoptosis-related pathways. Flow cytometry analysis was used to evaluate the level of apoptosis in GBM cells after treatment with GBEPPT and PPT (Figure 6g). The proportion of early apoptotic GBM cells increases significantly in comparison to the control. Subsequently, western blotting (WB) analysis of key apoptosis-related proteins confirms that both GBEPPT and PPT markedly induce apoptosis in GBM cells, resulting in the activation of the apoptotic executor protein caspase-3, as well as its downstream PARP protein (Figure 6h).

It is noted that the transcriptome sequencing does not capture any significant changes in the mitochondria-associated apoptotic pathway. The treatment of GBM cells with

GBEPPT may result in mild stress on the mitochondria, initiating the damage-repair processes. The expression level of KIF5B, an outward-motor protein required for mitochondrial mitocytosis,[18] is significantly elevated in the cells treated with GBEPPT, whereas its expression level in the PPT-treated group is not significantly different from that of the control group (Figure S77, Supporting Information).

We finally selected IDH-WT (isocitrate dehydrogenase wild type) GBM samples from a patient to build a de novo GBM model to assess the therapeutic effectiveness of GBEPPT against GBM. GBM in the frontoparietal lobe of the patient is confirmed from the enhanced MRI image (Figure 6i, Figure S78, Supporting Information). Fluorescent immunohistochemical staining of the GBM indicates high expression of GFAP, which highly overlaps with Ki67 (Figure S79, Supporting Information). After treatment with PPT or GBEPPT, patient-derived GBM cells exhibit evident microtubule disruption (Figure 6j) and distinct apoptosis (Figure S80 and S81, Supporting Information). These results suggest that GBEPPT could impose a potent therapeutic effect on clinical GBM, which is similar to that observed in the GBM model.

As the chemotherapeutic drug in the clinical standard of care (SOC) for GBM, temozolomide (TMZ) is currently facing challenge due to the insufficient effectiveness. Here, we constructed the GBEPPT nanomedicine to improve the therapeutic effect of a chemotherapeutic drug, PPT other than TMZ, for GBM treatment, although this chemotherapeutic agent has intrinsic issues, such as systemic toxicity, inability to penetrate the blood-brain barrier (BBB), and poor tumor tissue penetration. The construction of the PPT nanomedicine helps overcome these intrinsic issues and improve the therapeutic effect of the drug PPT, resulting in great survival benefits for the GBM mice. The advantages of GBEPPT in comparison with TMZ used in the GBM standard of care include: 1) Different treatment mechanisms between GBEPPT and TMZ. GBEPPT could be served as a supplementary or alternative therapeutic agent; 2) GBEPPT remarkably reduced the systemic toxicity of the antitumor drug PPT, and its effective therapeutic dose is significantly lower than that of TMZ; and 3) This nanomedicine platform has potential to accommodate different therapeutic or imaging

agents or their combinations. Compared to TMZ an anti-GBM drug, GBEPPT can produce synergistic effects after its combination with standard treatments such as surgery and radiotherapy. For example, through contrast-agent labelling, GBEPPT may provide a precise guidance for radiotherapy and exert an anti-tumor efficacy to the cells in surgical resection margins.

3. Conclusion

In summary, with the aid of DPD simulations, we have successfully developed an amphiphilic block polymer-drug conjugate, GBEPPT, to self-assemble into a nanomedicine with enhanced tumor accumulation and deep penetration through the BBB and the GBM tissue due to its GGT-activated charge reversal and mitochondrial disturbance-induced mitocytosis. Overexpressed GGT on the BBB neovasculature and tumor cell membranes facilitates charge reversal of GBEPPT from negative to positive, promoting its diffusion through the BBB and rapid internalization into GBM cells to target mitochondria. GBEPPT deposited in the mitochondria induces disturbance of the mitochondrial homeostasis, triggering the quality control process to transfer the disturbed mitochondria with GBEPPT to the extracellular region via mitocytosis. The exocytotic GBEPPT could be endocytosed by neighbor cells to accomplish intracellular-to-intercellular delivery of GBEPPT, augmenting its accumulation and promoting its deep penetration in the GBM tumor. Meanwhile, during the delivery process, GBEPPT is activated by GSH at a high concentration in the tumor microenvironment to release PPT to induce cell apoptosis, which remarkably enhances the anti-tumor effects on the GBM. Therefore, the subcellular targeting nanomedicine could be effectively delivered into weakly permeable malignancies through mitochondrial disturbance and active mitocytosis, offering great potential in combating brain tumors.

Supporting Information

Supporting Information is available from the Wiley Online Library or from the author.

Acknowledgements

Y.X. and B.W. contributed equally to this work. This work was supported by National Natural Science Foundation of China (82272644, 32271445, 51903173, 82372836), National Key Research and Development Program of China (2022YFC2009900), 1·3·5 Project for Disciplines of Excellence, West China Hospital, Sichuan University (ZYJC21013). The authors would like to thank the Analytical and Testing Center of Sichuan University for NMR spectroscopy and morphology characterization of the polymers by Prof. Pengchi Deng *et al*. The authors thank Qin-Fang Zhang (College of Chemistry at Sichuan University), Yaping Wu, Lei Wu, Lin Bai, Bo Su, Di Wang, Zhiqian Li, Zhengju Chen, Yang Yang, Xijing Yang, Qiaorong Huang, Xue Li and Wentong Meng (Histology and Imaging Platform, Huaxi MR Research Center, Experimental Animal Center of West China Hospital, Laboratory of Stem Cell Biology, West China Hospital, Sichuan University) for sample analysis, imaging, histological staining, cellular experiment and animal experiment, Wentao Feng and Xin Qi (Neurosurgery Research Laboratory, West China Hospital, Sichuan University) for patient-derived GBM study.

Conflict of Interest

The authors declare no conflict of interest.

References

[1] a) L. R. Schaff, I. K. Mellinghoff, *JAMA.* **2023**, 329, 574; b) M. Weller, M. van den Bent, M. Preusser, E. Le Rhun, J. C. Tonn, G. Minniti, M. Bendszus, C. Balana, O. Chinot, L. Dirven, P. French, M. E. Hegi, A. S. Jakola, M. Platten, P. Roth, R. Ruda, S. Short, M. Smits, M. Taphoorn, A. von Deimling, M. Westphal, R. Soffietti, G. Reifenberger, W. Wick, *Nat. Rev. Clin. Oncol.* **2021**, 18, 170; c) X.H. Gao, J. Qian, S.Y. Zheng, Y.Z. Changyi, J.Y. Zhang, S.H. Ju, J.H. Zhu, C. Li, *ACS Nano* **2014**, 8, 3678-3689; d) Y.Y. Wang, X.X. Wang, R.S. Xie, J.C. Burger, Y. Tong, S.Q. Gong, *Adv. Mater*. **2023**, 35, 2208018.

[2] a) M. Martin, S. Vermeiren, N. Bostaille, M. Eubelen, D. Spitzer, M. Vermeersch, C. P. Profaci, E. Pozuelo, X. Toussay, J. Raman-Nair, P. Tebabi, M. America, A. De Groote, L. E. Sanderson, P. Cabochette, R. Germano, D. Torres, S. Boutry, D. A. de Kerchove, E. J. Bellefroid, T. N. Phoenix, K. Devraj, B. Lacoste, R. Daneman, S. Liebner, B. Vanhollebeke, *Science* **2022**, 375, eabm4459; b) Y. Yao, J. Wang, Y. Liu, Y. Qu, K. Wang, Y. Zhang, Y. Chang, Z. Yang, J. Wan, J. Liu, H. Nakashima, S. E. Lawler, E. A. Chiocca, C. F. Cho, F. Bei, *Nat. Biomed. Eng.* **2022**,

6, 1257; c) Z. Mi, Q. Yao, Y. Qi, J. Zheng, J. Liu, Z. Liu, H. Tan, X. Ma, W. Zhou, P. Rong, *Acta Pharm. Sin. B* **2023**, 13, 819.

[3] a) M. Rullo, M. Cipolloni, M. Catto, C. Colliva, D. V. Miniero, T. Latronico, M. de Candia, T. Benicchi, A. Linusson, N. Giacche, C. D. Altomare, L. Pisani, *J. Med. Chem.* **2022**, 65, 3962; b) M. Goldsmith, L. Abramovitz, D. Peer, *ACS Nano* **2014**, 8, 1958; c) N. Kianinejad, Y. M. Kwon, *BioImpacts* **2023**, 13, 1.

[4] D. E. Tylawsky, H. Kiguchi, J. Vaynshteyn, J. Gerwin, J. Shah, T. Islam, J. A. Boyer, D. R. Boue, M. Snuderl, M. B. Greenblatt, Y. Shamay, G. P. Raju, D. A. Heller, *Nat. Mater.* **2023**, 22, 391.

[5] a) A. I. Minchinton, I. F. Tannock, *Nat. Rev. Cancer* **2006**, 6, 583; b) K. D. Pawlowski, J. T. Duffy, M. V. Babak, I. V. Balyasnikova, *Trends Mol. Med* **2023**, 29, 282.

[6] a) O. Tietz, F. Cortezon-Tamarit, R. Chalk, S. Able, K. A. Vallis, *Nat. Chem.* **2022**, 14, 284; b) J. Liang, L. Li, H. Tian, Z. Wang, G. Liu, X. Duan, M. Guo, J. Liu, W. Zhang, E. C. Nice, C. Huang, W. He, H. Zhang, Q. Li, *Small* **2023**, e2303073; c) J. Liu, Y. Sun, X. Zeng, Y. Liu, C. Liu, Y. Zhou, Y. Liu, G. Sun, M. Guo, *Adv. Mater.* **2023**, 35, e2303660.

[7] a) L. Gu, Z. Duan, X. Chen, X. Li, Q. Luo, A. Bhamra, D. Pan, H. Zhu, X. Tian, R. Chen, Z. Gu, H. Zhang, Z. Qian, Q. Gong, K. Luo, *Adv. Mater.* **2022**, 34, e2200048; b) L. Gu, Z. Duan, X. Li, X. Li, Y. Li, X. Li, G. Xu, P. Gao, H. Zhang, Z. Gu, J. Chen, Q. Gong, K. Luo, *Bioact. Mater.* **2023**, 26, 102.

[8] a) Y. Liu, J. Tan, Y. Zhang, J. Zhuang, M. Ge, B. Shi, J. Li, G. Xu, S. Xu, C. Fan, C. Zhao, *Biomaterials* **2018**, 173, 1; b) A. Toth, S. Veszelka, S. Nakagawa, M. Niwa, M. A. Deli, *Recent Pat CNS Drug Discov* **2011**, 6, 107.

[9] Y. Zou, Y. Sun, Y. Wang, D. Zhang, H. Yang, X. Wang, M. Zheng, B. Shi, *Nat. Commun.* **2023**, 14, 4557.

[10] a) H. Yan, P. Xu, H. Ma, Y. Li, R. Zhang, H. Cong, B. Yu, Y. Shen, *Biomaterials* **2023**, 301, 122213; b) Q. Zhou, S. Shao, J. Wang, C. Xu, J. Xiang, Y. Piao, Z. Zhou, Q. Yu, J. Tang, X. Liu, Z. Gan, R. Mo, Z. Gu, Y. Shen, *Nat. Nanotechnol.* **2019**, 14, 799; c) G. Wang, B. Wu, Q. Li, S. Chen, X. Jin, Y. Liu, Z. Zhou, Y. Shen, P. Huang, *Small* **2020**, 16, e2004172.

[11] a) Y. Yang, D. Hu, Y. Lu, B. Chu, X. He, Y. Chen, Y. Xiao, C. Yang, K. Zhou, L. Yuan, Z. Qian, *Acta Pharm. Sin. B* **2022**, 12, 2710; b) J. Zhao, C. Wang, W.B. Sun, C. Li, *Adv. Mater*. **2022**, 34, 2203667; c) H. Li, Y. Feng, Q. Luo, Z. Li, X. Li, H. Gan, Z. Gu, Q. Gong, K. Luo, *Theranostics* **2023**, *13*, 5386; d) J. Li, X. Zhang, M. Zhao, L. Wu, K. Luo, Y. Pu, B. He, *Biomacromolecules* **2018**, *19*, 3140; e) Y. Ou, K. Chen, H. Cai, H. Zhang, Q. Gong, J. Wang, W. Chen, K. Luo, *Biomater. Sci.* **2018**, *6*, 1177.

[12] a) X. Zheng, D. Pan, G. Zhu, L. Zhang, A. Bhamra, R. Chen, H. Zhang, Q. Gong, Z. Gu, K. Luo, *Adv. Mater.* **2022**, 34, e2201200; b) S. Zeng, X. Quan, H. Zhu, D. Sun, Z. Miao, L. Zhang, J. Zhou, *Langmuir* **2021**, 37, 1225; c) X. Zheng, D. Pan, X. Chen, L. Wu, M. Chen, W. Wang, H. Zhang, Q. Gong, Z. Gu, K. Luo, *Adv. Sci.* **2021**, 8, e2102741. d) X. Yang, Y. Wang, J. Zhao, H. Rong, Y. Chen, M. Xiong, X. Ye, S. Yu, H. Hu, *Acta Pharm. Sin. B* **2022**, 12, 3934.

[13] a) H. Gao, Z. Yang, S. Zhang, S. Cao, Z. Pang, X. Yang, X. Jiang, *J. Control. Release* **2013**, 172, 921; b) J. Ye, Y. Yang, J. Jin, M. Ji, Y. Gao, Y. Feng, H. Wang, X. Chen, Y. Liu, *Bioact. Mater.* **2020**, 5, 694; c) T. Zwain, J. E. Alder, B. Sabagh, A. Shaw, A. J. Burrow, K. K. Singh, *Mater. Sci. Eng. C-Mater. Biol. Appl.* **2021**, 121, 111774.

[14] a) W. Tang, W. Fan, J. Lau, L. Deng, Z. Shen, X. Chen, *Chem. Soc. Rev.* **2019**, 48, 2967; b) Z. Shen, T. Liu, Z. Yang, Z. Zhou, W. Tang, W. Fan, Y. Liu, J. Mu, L. Li, V. I. Bregadze, S. K. Mandal, A. A. Druzina, Z. Wei, X. Qiu, A. Wu, X. Chen, *Biomaterials* **2020**, 235, 119783; c) M. Gao, Y. Chen, C. Wu, *Bioengineered* **2021**, 12, 12263; d) J. Mo, L. He, B. Ma, T. Chen, *ACS Appl. Mater. Interfaces* **2016**, 8, 6811.

[15] a) Y. Wang, X. Wang, R. Xie, J. C. Burger, Y. Tong, S. Gong, *Adv. Mater.* **2023**, 35, e2208018; b) F. Shen, D. Tao, R. Peng, Y. He, Z. Liu, J. Ji, L. Feng, *Biomaterials* **2022**, 283, 121428.

[16] a) Y. Han, C. Gao, H. Wang, J. Sun, M. Liang, Y. Feng, Q. Liu, S. Fu, L. Cui, C. Gao, Y. Li, Y. Yang, B. Sun, *Bioact. Mater.* **2021**, 6, 529; b) S. Yoon, J. J. Rossi, *Adv. Drug Deliv. Rev.* **2018**, 134, 22; c) M. Furmanik, M. Chatrou, R. van Gorp, A. Akbulut, B. Willems, H. Schmidt, G. van Eys, M. L. Bochaton-Piallat, D. Proudfoot, E. Biessen, U. Hedin, L. Perisic, B. Mees, C. Shanahan, C. Reutelingsperger, L. Schurgers, *Circ. Res.* **2020**, 127, 911; d) Y. Liu, Y. Huo, L. Yao, Y. Xu, F. Meng, H. Li, K. Sun, G. Zhou, D. S. Kohane, K. Tao, *Nano Lett.* **2019**, 19, 8010; e) T. Cronqvist, L. Erlandsson, D. Tannetta, S. R. Hansson, *Placenta* **2020**, 100, 133; f) L. A. Mulcahy, R. C. Pink, D. R. Carter, *J. Extracell. Vesicles* **2014**, 3, 24641.

[17] a) H. Ishida, Y. Hirota, C. Genka, H. Nakazawa, H. Nakaya, T. Sato, *Circ. Res.* **2001**, 89, 856; b) N. A. Marcondes, S. R. Terra, C. S. Lasta, N. Hlavac, M. L. Dalmolin, L. A. Lacerda, G. Faulhaber, F. Gonzalez, *Cytom. Part A* **2019**, 95, 214; c) Y. Zhang, M. Xia, Z. Zhou, X. Hu, J. Wang, M. Zhang, Y. Li, L. Sun, F. Chen, H. Yu, *Int. J. Nanomed.* **2021**, 16, 283.

[18] H. Jiao, D. Jiang, X. Hu, Du W, L. Ji, Y. Yang, X. Li, T. Sho, X. Wang, Y. Li, Y. T. Wu, Y. H. Wei, X. Hu, L. Yu, *Cell* **2021**, 184, 2896.

[19] S. Pickles, P. Vigie, R. J. Youle, *Curr. Biol.* **2018**, 28, R170.

[20] a) L. Ma, Y. Li, J. Peng, D. Wu, X. Zhao, Y. Cui, L. Chen, X. Yan, Du Y, L. Yu, *Cell Res.* **2015**, 25, 24; b) D. Jiang, Z. Jiang, D. Lu, X. Wang, H. Liang, J. Zhang, Y. Meng, Y. Li, D. Wu, Y. Huang, Y. Chen, H. Deng, Q. Wu, J. Xiong, A. Meng, L. Yu, *Nat. Cell Biol.* **2019**, 21, 966; c) Y. Jiang, X. Liu, J. Ye, Y. Ma, J. Mao, D. Feng, X. Wang, *Cell Commun. Signal.* **2023**, 21, 105.

[21] a) C. Wang, Du W, Q. P. Su, M. Zhu, P. Feng, Y. Li, Y. Zhou, N. Mi, Y. Zhu, D. Jiang, S. Zhang, Z. Zhang, Y. Sun, L. Yu, *Cell Res.* **2015**, 25, 1108; b) R. Queiroz, T. Smith, E. Villanueva, M. Marti-Solano, M. Monti, M. Pizzinga, D. M. Mirea, M. Ramakrishna, R. F. Harvey, V. Dezi, G. H. Thomas, A. E. Willis, K. S. Lilley, *Nat. Biotechnol.* **2019**, 37, 169.

[22] a) L. Zhou, T. Zhang, W. Shao, R. Lu, L. Wang, H. Liu, B. Jiang, S. Li, H. Zhuo, S. Wang, Q. Li, C. Huang, D. Lin, *Skelet. Muscle* **2021**, 11, 17; b) X. Liu, J. Miao,

C. Wang, S. Zhou, S. Chen, Q. Ren, X. Hong, Y. Wang, F. F. Hou, L. Zhou, Y. Liu, *Kidney Int.* **2020**, 97, 1181.

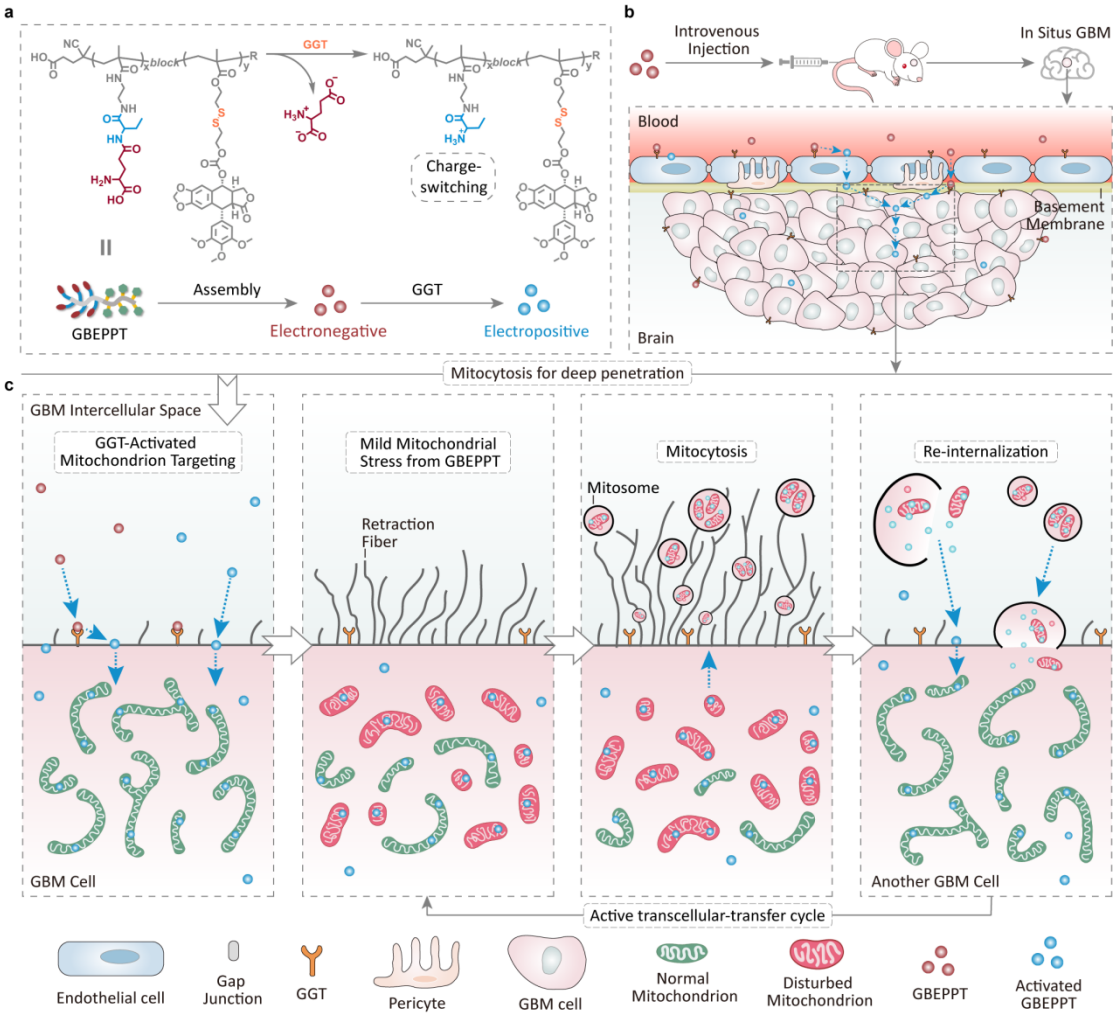
[23] a) S. Faletti, D. Osti, E. Ceccacci, C. Richichi, B. Costanza, L. Nicosia, R. Noberini, G. Marotta, L. Furia, M. R. Faretta, S. Brambillasca, M. Quarto, L. Bertero, R. Boldorini, B. Pollo, S. Gandini, D. Cora, S. Minucci, C. Mercurio, M. Varasi, T. Bonaldi, G. Pelicci, *Sci. Transl. Med.* **2021**, 13, eabf7036; b) T. Jiang, Y. Qiao, W. Ruan, D. Zhang, Q. Yang, G. Wang, Q. Chen, F. Zhu, J. Yin, Y. Zou, R. Qian, M. Zheng, B. Shi, *Adv. Mater.* **2021**, 33, e2104779.

[24] T. Nishihara, H. A. Yoshihara, H. Nonaka, Y. Takakusagi, F. Hyodo, K. Ichikawa, E. Can, J. A. Bastiaansen, Y. Takado, A. Comment, S. Sando, *Angew. Chem. Int. Ed. Engl.* **2016**, 55, 10626.

[25] a) A. S. Vore, T. M. Barney, M. M. Deak, E. I. Varlinskaya, T. Deak, *Brain. Behav. Immun.* **2022**, 102, 209; b) S. Alikunju, P. M. Abdul Muneer, Y. Zhang, A. M. Szlachetka, J. Haorah, *Brain, Behavior, and Immunity* **2011**, 25, S129.

[26] a) W. Zhao, Y. Cong, H. M. Li, S. Li, Y. Shen, Q. Qi, Y. Zhang, Y. Z. Li, Y. J. Tang, *Nat. Prod. Rep.* **2021**, 38, 470; b) X. Zhang, K. P. Rakesh, C. S. Shantharam, H. M. Manukumar, A. M. Asiri, H. M. Marwani, H. L. Qin, *Bioorg. Med. Chem.* **2018**, 26, 340.

[27] R. L. Margolis, L. Wilson, *Cell* **1978**, 13, 1.



Scheme 1. Mitocytosis to enhance intercellular transfer of GBEPPT for GBM treatment. a) Enzyme-activated structural transformation of GBEPPT, and schematic illustration of self-assembly and charge reversal processes. b) Treatment of *in situ* GBM with enhanced accumulation and penetration. c) The mitocytosis process mediates active transcellular transport of GBEPPT for deep penetration. GBEPPT with a positive charge specifically targets mitochondria to disturb the mitochondrial homeostasis and mediate mitocytosis. During the mitocytosis process, mitosomes that contain the disturbed mitochondria and the nanomedicine are expelled out of the cell. Subsequently, the nanomedicine from the mitosomes could be reinternalized by neighboring GBM cells. In this process, the mitochondria act as a relay station to continuously mediate the transcytosis of the nanomedicine.

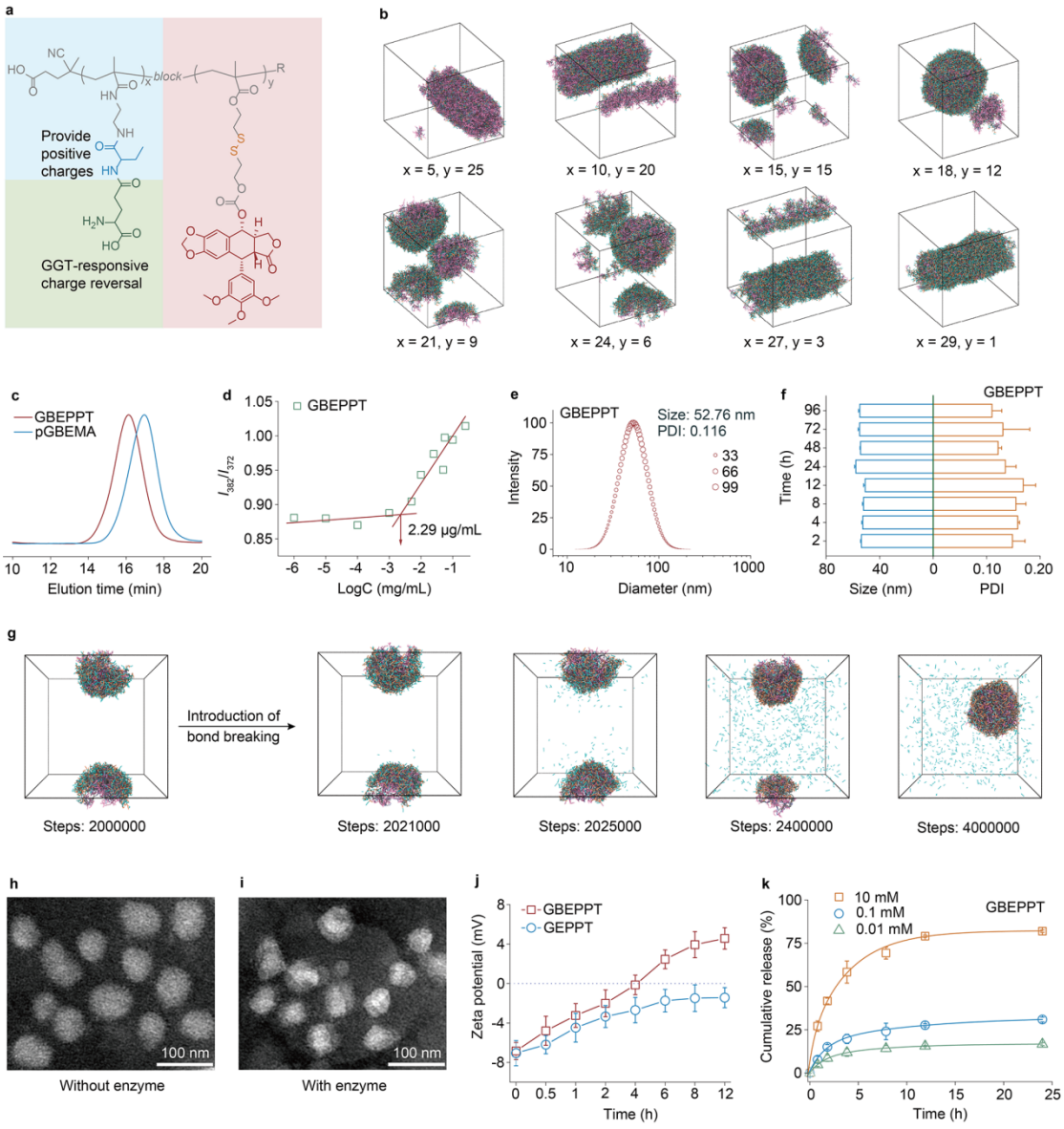


Figure 1. DPD simulations and physicochemical characterizations of GBEPPT. a) Structure of pGBEMA-*b*-pSSPPT (GBEPPT). GBEPPT is composed of a hydrophilic unit containing a GGT-responsive charge-reversal segment (γ-glutamine) that is conjugated to a positive-charge provider (aminobutyric acid), and a hydrophobic domain containing a GSH-responsive linker to connect an anti-tumor drug (PPT) with the hydrophobic unit. b) Molecular morphologies of GBEPPT after self-assembly via DPD simulations. Side views of GBEPPT in H_2O at different hydrophilic-hydrophobic ratios. x and y are hydrophilic and hydrophobic units, respectively. c) Gel permeation chromatography (GPC) chromatograms of pGBEMA and GBEPPT. d) Critical micelle concentration (CMC) of GBEPPT. e) Hydrodynamic size and polydispersity index

(PDI) of GBEPPT via DLS. f) Stability of GBEPPT in PBS. g) Dissociation of γ-glutamoyl from GBEPPT via DPD simulations. Sectional views of GBEPPT in a bond breaking process at different simulation steps. TEM images of GBEPPT (h) without or (i) with enzymatic incubation. j) Zeta potentials of GBEPPT and GEPPT in the presence of 10 U mL^{-1} GGT at 37 °C. k) Drug release profiles of GBEPPT in the presence of GSH at different concentrations.

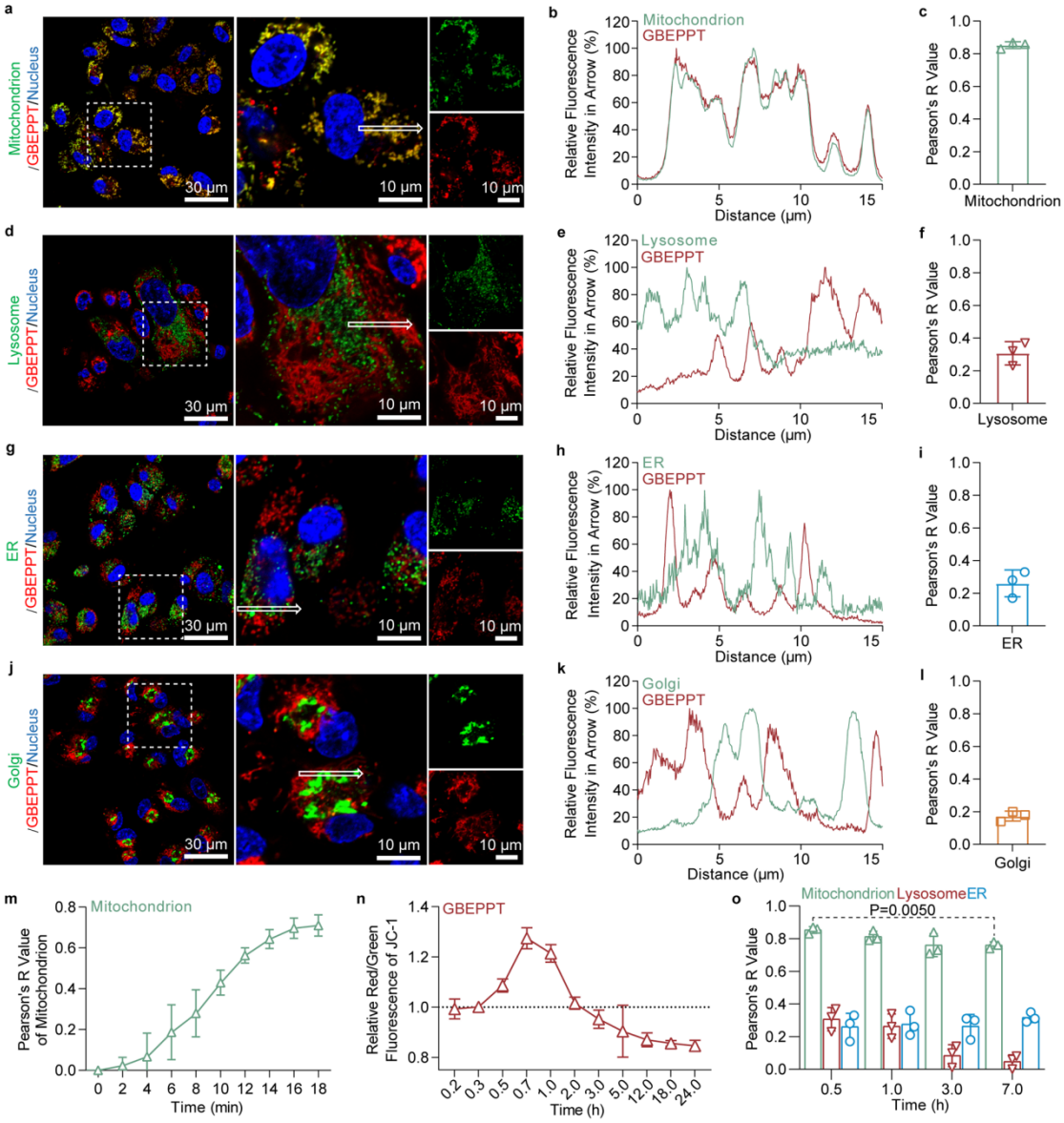


Figure 2. Co-localization of GBEPPT with mitochondria in GBM cells. a-c) Fluorescent images for co-localization of GBEPPT and mitochondria, semi-quantitative analysis of the fluorescence signal of GBEPPT and mitochondria, and the

Pearson correlation coefficient (Pearson's R) for co-localization of GBEPPT and mitochondria. Red for GBEPPT, green for mitochondria, blue for nuclei, and yellow for overlapping of red and green. d-f) Fluorescent images for co-localization of GBEPPT and lysosomes, semi-quantitative analysis of the fluorescence signal of GBEPPT and lysosomes, and the Pearson correlation coefficient for co-localization of GBEPPT and lysosomes. Red for GBEPPT, green for lysosomes, blue for nuclei, yellow for overlapping of red and green. g-i) Fluorescent images for co-localization of GBEPPT and the endoplasmic reticulum, semi-quantitative analysis of the fluorescence signal of GBEPPT and the endoplasmic reticulum, and the Pearson correlation coefficient for co-localization of GBEPPT and the endoplasmic reticulum. Red for GBEPPT, green for endoplasmic reticulum, blue for nuclei, yellow for overlapping of red and green. j-l) Fluorescent images for co-localization of GBEPPT and the Golgi apparatus, semi-quantitative analysis of the fluorescence signal of GBEPPT and the Golgi apparatus, and the Pearson correlation coefficient for co-localization of GBEPPT and the Golgi apparatus. Red for GBEPPT, green for Golgi apparatus, blue for nuclei, yellow for overlapping of red and green. m) Pearson's R for co-localization of GBEPPT and mitochondria within 0-18 min. n) Semi-quantitative analysis of the JC-1 fluorescence signal in GBEPPT-treated GBM cells. o) Pearson's R for co-localization of GBEPPT and mitochondria at 0.5, 1, 3 and 7 h.

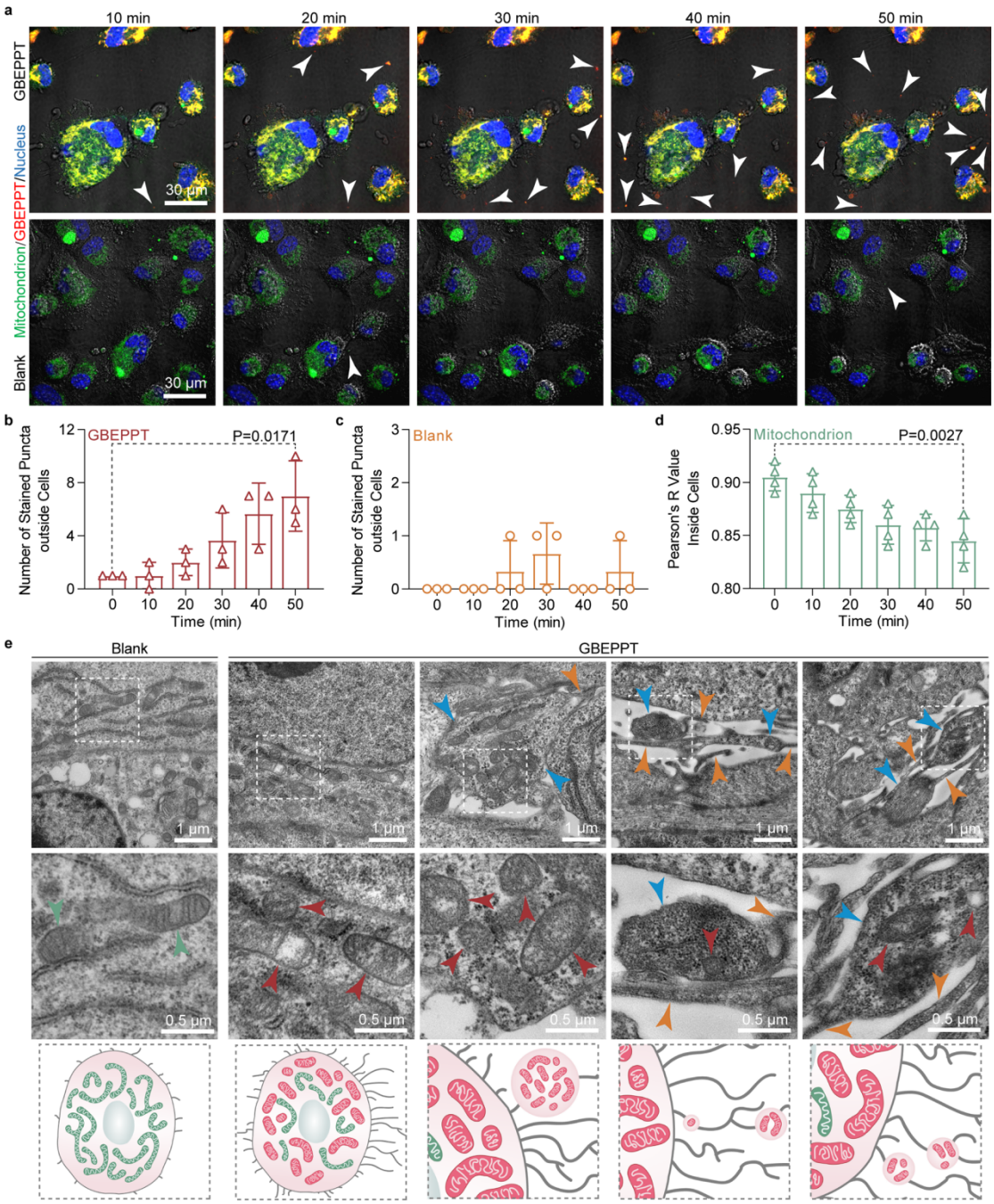


Figure 3. GBEPPT-mediated mitocytosis of GBM cells. a) Dynamic changes in mitochondrial exocytosis by the GBM cells after co-incubation with GBEPPT for 1 h, which is highlighted by white arrows. Green for mitochondria, red for GBEPPT, blue for nuclei, and yellow for overlapping of green and red. Semi-quantitative analysis of the number of puncta secreted from GBM cells that were stained with both red and green fluorescence in (b) the GBEPPT-treated group and (c) the control group. d) Dynamic changes in the Pearson's R for co-localization of mitochondria and GBEPPT

inside GBM cells after GBEPPT treatment. e) TEM images of normal mitochondria (green arrow) in the control group, and disturbed mitochondria (red arrow) in the GBEPPT-treated group. Typical mitosomes (blue arrow) contain disturbed mitochondria (red arrow) and retraction fibers (orange arrow) after treatment of GBM cell with GBEPPT.

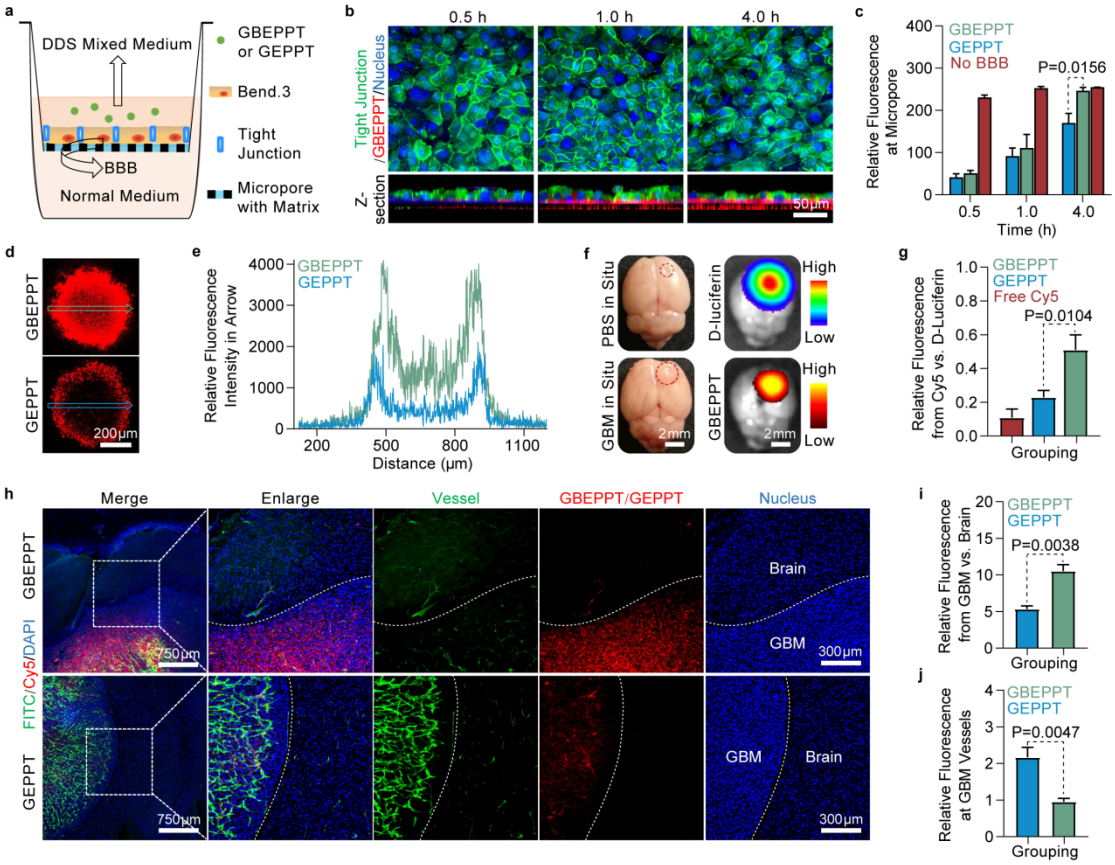


Figure 4. Penetration of GBEPPT through the BBB and the solid GBM tissue. a) Schematic drawing of an in vitro BBB model. b) Fluorescence images for the BBB model after co-incubation with GBEPPT for 0.5, 1 and 4 h. Green for T junctions, red for GBEPPT, and blue for nuclei. c) Semi-quantitative analysis of the fluorescence signal in the micropores of the Z-section of the BBB model treated with GBEPPT or GEPPT, or the transwell without the BBB treated with GBEPPT. d) CLSM images of large-diameter GBM MTSs after co-incubation with GBEPPT or GEPPT for 6 h and (e) semi-quantitative analysis of the fluorescence signal intensity along the arrows from the left to the right periphery of MTSs. f) Mouse brain tissues injected with PBS (Upper Left) and GBM (Lower Left) in-situ, and fluorescence images of the same mouse brain

with GBM after intravenous injection of D-Luciferin (Upper Right) and GBEPPT (Lower Right). g) Semi-quantitative analysis of the level of accumulation of the free Cy5, GEPPT and GBEPPT in the GBM tissue. h) Fluorescence images of sections including both brain and GBM tissues. Green for FITC-dextran labelled blood vessels, red for Cy5-labelled GBEPPT, and blue for DAPI-stained nuclei. Semi-quantitative analysis of the accumulation level of GBEPPT and GEPPT in the GBM tissue (i) and in the neovascular within the GBM tissue (j) compared to that at the brain tissue.

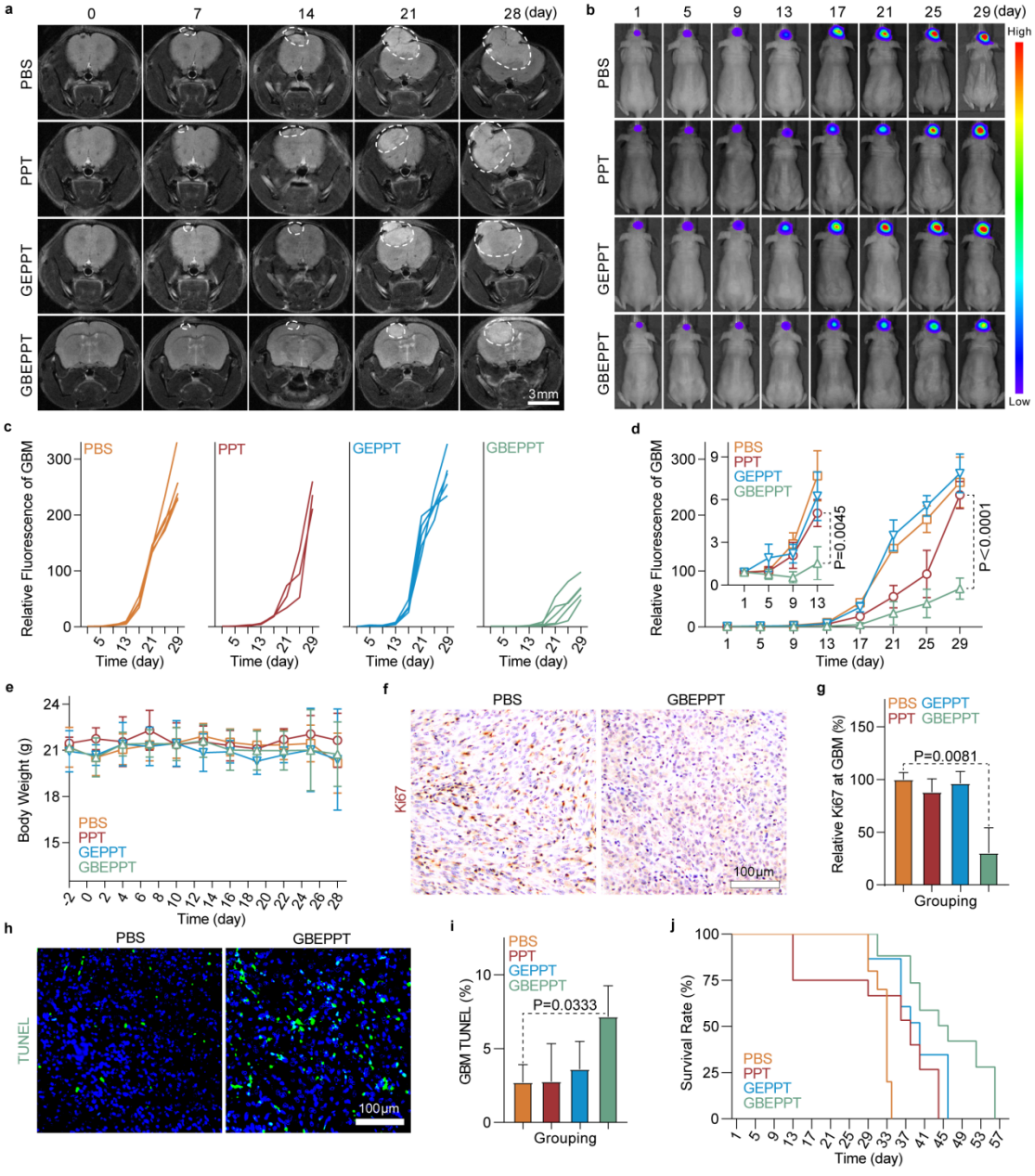


Figure 5. Enhanced therapeutic effects on in-situ GBM tumors by GBEPPT. a) In-situ GBM tumor growth in the mice treated with PBS, PPT, GEPPT, and GBEPPT monitored by 7T MRI. b) In-situ GBM tumor growth in the mice treated with PBS, PPT, GEPPT, and GBEPPT monitored by live fluorescence imaging. c) Semi-quantitative analysis of in-situ GBM tumor growth in each group. d) Averaged in-situ GBM tumor growth rates in four groups. e) Body weight changes in the GBM mice. f) Images of Ki67-stained histological sections of in-situ GBM tumors and (g) semi-quantitative analysis of the Ki67 signal intensity. h) Images of TUNEL-stained histological sections of in-situ GBM tumors and (i) semi-quantitative analysis of the TUNEL signal intensity. j) Survival analysis of the mice with in-situ GBM tumors after treatment with PBS, PPT, GEPPT, and GBEPPT.

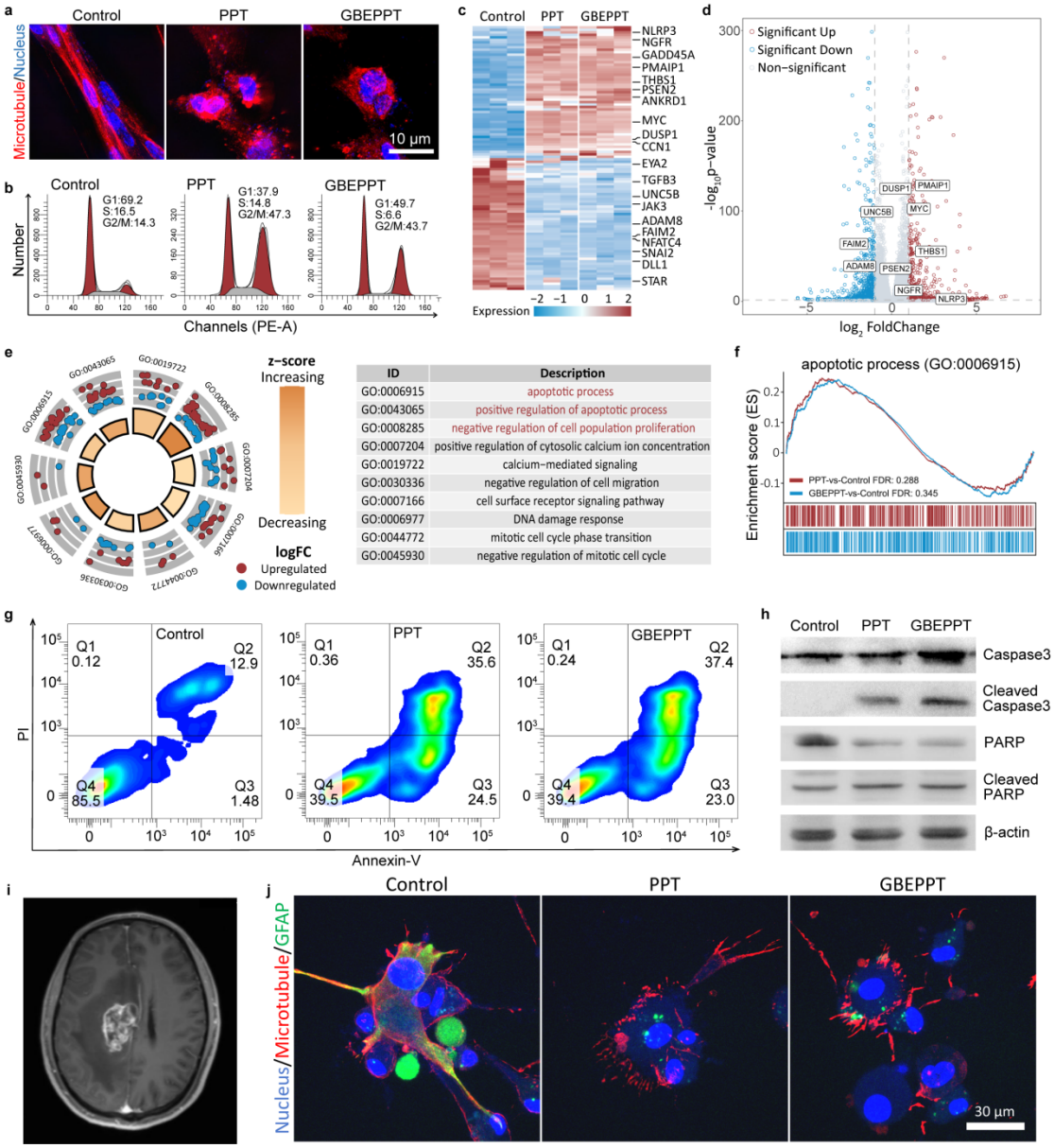


Figure 6. GBEPPT induces apoptosis via cell cycle arrest and disruption of microtubule structures. a) The morphology of microtubules in the U-87 cells treated with PPT and GBEPPT and (b) flow cytometry analysis of their cell cycle arrest. c) Heatmap for differential gene expression levels in GBM cells after different treatments. d) Volcano plot of gene expression in GBEPPT-treated GBM cells. e) GO enrichment analysis of gene expression in GBM cells after GBEPPT treatment. f) GSEA analysis of the apoptosis process (GO:0006915) in the groups treated with PPT and GBEPPT. g) Flow cytometry analysis of the level of apoptosis in the GBM cells treated with PPT and GBEPPT and (h) the apoptosis-related protein expression levels in the GBM cells

measured by Western blotting. i) Enhanced cross-sectional MRI image of GBM in the frontal parietal lobe of the patient. Clinical GBM samples were obtained from the patient. j) Microtubule morphological changes in patient-derived GBM cells after treatment with PPT and GBEPPT.

Table of Contents

An enzyme-activable mitochondrion-disturbing nanomedicine assembled from an amphiphilic block polymer-drug conjugate is developed for achieving efficient BBB crossing and deep GBM penetration. This nanomedicine interferes mitochondrial homeostasis, which mediates the process of mitocytosis for mitochondrial quality control, facilitating mitosome-mediated active transcellular transport in GBM tissues.

Keywords: Nanomedicine, mitochondrion targeting, mitocytosis, tumor penetration, glioblastoma

Yufan Xiang, Bing Wang, Wanchun Yang, Xiuli Zheng, Rongjun Chen, Qiyong Gong, Zhongwei Gu, Yanhui Liu and Kui Luo**

Mitocytosis mediated by an enzyme-activable mitochondrion-disturbing polymer-drug conjugate enhances active penetration in glioblastoma therapy

ToC figure

